Defect Engineering by Codoping in KCaI_{3}:Eu^{2+} Single-Crystalline Scintillators

Yuntao Wu, Qi Li, Steven Jones, Chaochao Dun, Sheng Hu, Mariya Zhuravleva, Adam C. Lindsey, Luis Stand, Matthew Loyd, Merry Koschan, John Auxier, II, Howard L. Hall, and Charles L. Melcher

Phys. Rev. Applied **8**, 034011 — Published 15 September 2017
DOI: 10.1103/PhysRevApplied.8.034011

Defect engineering by codoping in $KCaI_3:Eu^{2+}$ single-crystalline scintillators

Yuntao Wu,[1,2,]* Qi Li,[3,4,]* Steven Jones,[5] Chaochao Dun,[6] Sheng Hu,[7] Mariya Zhuravleva,[1,2] Adam C. Lindsey,[1,2] Luis Stand,[1,2], Matthew Loyd,[1,2] Merry Koschan,[1] John Auxier II,[5] Howard L. Hall,[5] and Charles L. Melcher [1,2]

[1]*Scintillation Materials Research Center*, [2]*Department of Materials Science and Engineering, University of Tennessee, Knoxville, Tennessee 37996, USA*
[3]*Physical Science Division, IBM Thomas J Watson Research Center, Yorktown Heights, NY 10598, USA*
[4]*Department of Computer Science, University of Illinois at Urbana-Champaign, Urbana, IL 61801, USA*
[5]*Department of Nuclear Engineering, University of Tennessee, Knoxville, Tennessee 37996, USA*
[6]*Department of Physics, Wake Forest University, Winston-Salem, NC 27109, USA*
[7]*Department of Chemical and Biomolecular Engineering, University of Tennessee, Knoxville, Tennessee 37996, USA*

Eu^{2+} doped alkali or alkali earth iodide scintillators with energy resolutions ≤3% at 662 keV promise the excellent discrimination ability for radioactive isotopes required for homeland security and nuclear non-proliferation applications. To extend their applications to X-ray imaging, such as computed tomography scans, the intense afterglow which delays the response time of such materials is an obstacle that needs to be overcome. However, a clear understanding of the origin of the afterglow and feasible solutions is still lacking. In this work, we present a combined experimental and theoretical combined investigation of the physical insights of codoping-based defect engineering which can reduce the afterglow effectively in $KCaI_3:Eu^{2+}$ single crystal scintillators. We illustrate that Sc^{3+} codoping greatly suppresses the afterglow, whereas Y^{3+}, Gd^{3+}, or La^{3+} codoping enhances the afterglow. Meanwhile, a light yield of 57,000 photons/MeV and an energy resolution of 3.4% at 662 keV can be maintained with the appropriate concentration of Sc^{3+} codoping, which makes the material promising for medical imaging applications. Through our thermoluminescence techniques and density functional theory calculations, we are able to identify the defect structures and understand the mechanism by which codoping affects the scintillation performance of $KCaI_3:Eu^{2+}$ crystals. The proposed defect-engineering strategy was further validated by achieving afterglow suppression in Mg^{2+} codoped $KCaI_3:Eu^{2+}$ single crystals.

INTRODUCTION

Scintillating materials that efficiently absorb radiation and convert it into pulses of light with a wavelength in or around the visible spectral region have been applied for more than a century in the discovery of X-rays, α-particles, β-particles, γ-rays, and recently in the quest for the Higgs boson. [1] The 2013 Nobel prize in physics was awarded jointly to François Englert and Peter Higgs "for the theoretical discovery of a mechanism that contributes to our understanding of the origin of mass of subatomic particles, and which recently was confirmed through the discovery of the predicted fundamental particle, by the ATLAS and CMS experiments at CERN's Large Hadron Collider". [2] The usage of almost 80,000 lead tungstate ($PbWO_4$) crystals for the electromagnetic calorimeter of the CMS experiment affirms the significant contribution of inorganic scintillators. Apart from the high-energy physics applications, inorganic scintillators are also widely used for radiation detection, medical imaging, oil well logging, and homeland security applications due to the high density and high atomic number compared to gas detectors and organic scintillators. [3] These various applications require scintillators to have suitable luminescent properties when used in different areas. As an example, X-ray based computed tomography (CT) requires the scintillators to have fast response time. On the other hand, the growing deployment of nuclear detection systems for the detection of illicit trafficking of nuclear materials demands excellent radioisotope identification ability. The ever-changing detection technology triggers an increasing demand of novel inorganic scintillators with enhanced energy resolution and light yield performances. [4,5] Some recently discovered notable scintillators with energy resolution ≤ 3% at 662 keV and light yield over 60,000 photons/MeV, all of which are halides, include $LaBr_3:Ce^{3+}$, [6] $SrI_2:Eu^{2+}$, [7] $KSr_2I_5:Eu^{2+}$, [8] $CsSrI_3:Eu^{2+}$, [9-11] $KCaI_3:Eu^{2+}$, [12] and $KCa_{0.8}Sr_{0.2}I_3:Eu^{2+}$. [13-15]

The promising scintillation properties of the halide materials mentioned above can be attributed to a combined result of the electronic structure of the host materials and the high luminescence efficiency of activators. Three main factors contribute to the high light yield: i) the narrower band-gaps of bromides and iodides compared to chlorides, fluorides or oxides; ii) higher luminescence efficiency of Eu^{2+} and Ce^{3+} activators; iii) large enough ionization energy to prevent undesired thermal quenching of the electrons trapped on the activators, such as 0.39±0.07 eV for $SrI_2:Eu^{2+}$ [16] and 1.15 eV for $KCaI_3:Eu^{2+}$. [13] For scintillators with a high light yield over 60,000 photons/MeV, the energy resolution used for detection devices is mainly limited by the non-proportional scintillation response. [17] For the halides mentioned above, the narrow and less dispersive top of the valence band favors the formation of the self-trapping of holes (STH) after excitation which is partly responsible for the high light yield in such materials. [18] For the hole self-trapping scintillators, a limitation on the diffusion of hot electrons can reduce the nonradiative transition of excitations on the localized defects, therefore improving the scintillation non-proportionality (nPR) of these materials. [19] Additionally, the nPR can be improved by an overall reduction of free carrier Auger quenching by reducing the free carrier density via codoping techniques. [20,21]

With respect to broadening the application of these high performance Eu^{2+} doped iodides from radioisotope identification to medical imaging, such as computed tomography (CT), strong afterglow is the major obstacle. The afterglow level drops less than two orders of magnitude after X-ray cutoff in the time scale of few hours. [10,13,22] To the best of our knowledge, only rather limited studies have been previously reported on: i) the origins of the defects responsible for the afterglow and ii) some feasible solutions for reducing the concentration of the associated electron traps in these Eu^{2+} doped iodides. For existing scintillation materials used for medical imaging applications, there has been promising success in afterglow improvement using either cation-alloying to lower the synthesis temperature [23] or codoping with aliovalent ions to avoid/reduce the impact of deleterious defects. [24-33] Recent experiments revealed that the oxygen vacancy induced afterglow in $Lu_2SiO_5:Ce^{3+}$ single crystals can be effectively suppressed by Gd^{3+} admixture because of the lower melting point. [23] Codoping with aliovalent ions, as another effective strategy, has been successfully applied for afterglow suppression, as in $CsI:Tl^+$ codoped with Eu^{2+}, [24] Sm^{3+}, [25,26] or Yb^{2+}, [27] and orthosilicates or aluminum garnets codoped with Ca^{2+} or Mg^{2+}. [28-33]

In the past six years, a series of Eu^{2+} doped halide scintillators in the ABX_3 (A = Cs, K; B = Ca, Sr; X = Cl, Br, I) perovskite-structure family were developed because of their attractive scintillation properties. Among these materials, $KCaI_3:Eu^{2+}$ has the best performance with respect to light yield and energy resolution. [12] By using Sr^{2+}-alloying, the afterglow level in $KCaI_3:Eu^{2+}$ was decreased and attributed to the reduced melting point, but the suppression effect is quite limited. [13] In this work, the afterglow is reduced by orders of magnitude by a codoping strategy, and the physical explanation is proposed from experimental and theoretical insights. The paper is organized as follows. First, we introduce the Bridgman growth of the $K(Ca_{0.97}Eu_{0.03})I_3$ single crystals codoped with M^{3+} (M=Sc, Y, Gd, or La), and the optical absorption and X-ray excited luminescence properties of these crystals. Second, the effects of the codopant on the scintillation properties are comprehensively investigated, including light yield, energy resolution, scintillation decay, non-proportionality, and X-ray induced afterglow. Finally, by using the thermoluminescence technique and first-principles calculations, we discuss the origins of intrinsic and extrinsic electron traps as well as the mechanism of codoping-induced afterglow variation.

EXPERIMENTAL AND THEORETICAL METHODS

Crystal Growth. We used the vertical Bridgman technique to grow noncodoped $K(Ca_{0.97}Eu_{0.03})I_3$ and $K(Ca_{0.97}Eu_{0.03})I_3$ codoped with 0.1 or 0.5 at% M (M=Sc^{3+}, Y^{3+}, Gd^{3+}, La^{3+}, or Mg^{2+}) single crystals. The codopant concentrations given refer to the initial starting melt, and calculations are based on the assumption that the codopants substituted for Ca based on atomic-size matching. High-purity anhydrous KI, CaI_2 and EuI_2 beads (5N) from APL Engineered Materials Inc. and $ScBr_3$, YBr_3, $GdBr_3$, $LaBr_3$, and $MgBr_2$ beads (4N) from Sigma-Aldrich were used. These beads were loaded and mixed in the quartz ampoules according to the particular composition. The loaded ampoule was evacuated to 10^{-6} torr and heated to 250°C and kept for 12 h at this temperature to remove residual water and oxygen impurities. After baking, the ampoule was sealed and transferred to a Bridgman growth furnace. We used a temperature gradient of ~25 °C/cm and a translation rate of 0.5 mm/h. The ∅13 or 15 mm grown crystals were cooled to room temperature (RT) at a speed of 10 °C/h. The grown crystals were taken out from ampoules, cut and polished in a glovebox with H_2O level of <0.1 ppm and O_2 level of <0.1 ppm. For each boule, a 2 mm thick sample for optical measurements and 5×5×5 mm cubic samples for the measurements of Eu^{2+} and codopant concentration, scintillation properties and thermoluminescence were extracted from the initial cylindrical region near the first-to-freeze region. These samples are transparent and inclusion-free. For optical and scintillation measurements, a crystal sample was loaded into a homemade housing filled with mineral oil that protects the sample from degradation. The housing was made of a quartz tube and a borosilicate glass as optical window. The sample handling process was conducted in a glovebox with H_2O level of <0.1 ppm and O_2 level of <0.1 ppm.

X-ray Diffraction (XRD) Measurements. A Bruker D2 Phaser with an X-ray source operated at 30 kV and 10 mA using a copper target which produced K-alpha emission lines detected by a 1-dimensional LYNXEYE detector was used to confirm the phase purity. The crystal samples were grounded into powders, and then loaded into a protective Kapton amorphous polymer domed sample stage that protects the sample from decomposition in ambient air during XRD measurement. The handling process was conducted in a glovebox with H_2O level of <0.1 ppm and O_2 level of <0.1 ppm. For these samples, all reflection peaks were in good agreement with the reference pattern of $KCaI_3$, which indicated the phase purity of the synthesized compounds.

Inductively Coupled Plasma Mass Spectrometry (ICP-MS) Measurements. The Eu, Sc, Y, Gd, and La concentrations in the crystals were measured using a GBC Scientific Optimass 9500 ICP-TOF-MS. Samples were prepared by dissolving each crystal in ASTM Type I water, and dilution to 10 μg/ mL. All samples also contained Ultra Trace 2% HNO_3 (JT Baker) to ensure complete dissolution of the analytes. A set of standards, prepared using serial dilution was created from Inorganic Ventures Rare Earth CCS-1 ICP−MS and IVStock-21 Multi-Element standards to quantify the signal using a linear least-square analysis. The nebulizer flow rate was set to 0.975 L/min, and the skimmer voltage to −1100 V. The data was collected in three replicates, each using a 30 second acquisition time.

Optical Property Measurements. Optical absorption spectra were measured with a Varian Cary 5000 UV-VIS-NIR spectrophotometer in the 350–800 nm range.

Scintillation Property Measurements. An X-ray tube operated at 35 kV, and 0.1 mA was used as an excitation source for X-ray excited radioluminescence (RL) measurements. Scintillation decay times were acquired with an Agilent DSO6104A digital oscilloscope in single shot mode under ^{137}Cs source irradiation.

Absolute light yield measurements were recorded by using a pulse processing chain consisting of a Hamamatsu R2059 photomultiplier tube (PMT) operated at -1500 V_{bias}, an Ortec 672 Amp, a Canberra model 2005 pre-Amp and a Tukan 8k multi-channel analyzer. Each sample was directly coupled to the PMT using mineral oil, and a dome-shaped Spectralon reflector with a 50 mm radius was used to maximize the collection of light. The photoelectron yields were estimated by using the single photoelectron peak method. Measurements on the samples were made with 10 μs shaping time for current pulse integration. Each sample was measured under irradiation with a 15 μCi ^{137}Cs source. The reproducibility of the LY measurements is ±5%.

The energy resolution was measured by using a 2-inch diameter high quantum efficiency Hamamatsu R6231-100 PMT. This PMT was operated at -1000 V_{bias}. ^{137}Cs (662 keV) and ^{57}Co (122 keV) γ-ray sources were used to irradiate the crystals. The energy resolution (ER) was calculated as the full width at half maximum (FWHM) divided by the photopeak centroid. Nonproportionality (nPR) was also evaluated with the same setup. Discrete ^{133}Ba (31 and 356 keV), ^{241}Am (59.5 keV), ^{57}Co (122 keV), ^{22}Na (511 keV), and ^{137}Cs (662 keV) X- and γ-ray sources were used to excite the crystals at energies from 31 to 662 keV.

Thermoluminescence measurements. For each thermoluminescence (TL) measurement, a 5×5×5 mm cube sample was transferred from a glovebox by using a sealed amber jar, and then quickly taken out and mounted on the cold finger of the cryostat. The pressure was reduced to 20 mTorr, and the sample was then heated to 600 K to ensure that all traps were empty in the temperature range of interest. The samples were cooled to 5 K and irradiated by an X-ray generator (X-ray Model; CMX003) at 35 kV and 0.1 mA for 3 min. Subsequently, the sample was again heated to 600 K at a rate of 9 K/min; noise due to thermionic emissions precluded the acquisition of high-quality data above this temperature. A Hamamatsu H3177 PMT optically coupled to the cryostat's light transport interface was used to measure the spectrally unresolved emission from the sample. The PMT current signal was transformed into a voltage signal using standard NIM electronics. A National Instruments 6002-E data acquisition card was then used to digitize this voltage signal. Software developed in-house was used to correlate the sample temperature with the signal intensity.

Computational methodology. Our density functional calculations were carried out using the QUANTUM ESPRESSO (QE) package [34] with norm-conserving pseudopotentials and generalized gradient approximation (GGA) exchange-correlation functionals parameterized by Perdew-Burke-Enzerhof (PBE). [35] A self-consistency convergence criterion of 10^{-8} eV was used for all calculations. All the structures were fully relaxed until the force components on any atoms were less than 10^{-3} eV/Å. The number of plane-waves was determined by a kinetic energy cutoff of 300 eV. Monkhorst-Pack grids with a maximum separation of 0.04 $Å^{-1}$ between k-points were used for sampling the Brillouin zone. [36] This sampling density was checked with respect to the convergence of the bulk $KCaI_3$ total energy, corresponding to a 6×2×2 k-point grid for the reciprocal space of a 20 atom $KCaI_3$ primitive cell. DFT+U type on-site potentials [37] were included for Sc-3d, Y-4d, La-4f, Gd-4f states, the U parameters were determined by the constrained random phase approximation described in Refs. 38 and 39. All the defect structures were simulated in a 4×1×1 80-atom supercell.

At thermodynamic equilibrium, the concentration of each type of defect follows the Boltzmann distribution [40]:

$$c = c_0 \exp\left(-\frac{\Delta G_{\mathrm{f}}}{k_{\mathrm{B}} T}\right) \quad (1)$$

where c_0 denotes the concentration of possible defect sites, k_{B} is the Boltzmann constant, and T is the temperature. Here we took the temperature (797 K) under which the crystal was grown. In this work, we approximated the formation free energy ΔG_{f} by the formation energy ΔE_{f}, given that the vibrational entropy contribution and the pressure-volume term are small.

The defect formation energies were calculated by [41,42]

$$\Delta E_{\mathrm{f}} = E_{\mathrm{def}} - E_{\mathrm{lat}} + q(\epsilon_{\mathrm{VBM}} + \mu_{\mathrm{e}}) - \sum_i \Delta n_i \mu_i \quad (2)$$

where E_{def} is the total energy of the lattice with the defect, E_{lat} is the total energy of the ideal host lattice with the same size. q is the charged state of the defect, and μ_e stands for the electron chemical potential, measured with respect to the valance band minimum ϵ_{VBM}. Δn_i stands for the difference between the number of atoms of type i in the defective lattice and the host lattice. The chemical potential μ_i of constituent i can be expressed as:

$$\mu_i = \mu_i^{\mathrm{bulk}} + \Delta\mu_i \quad (3)$$

where μ_i^{bulk} is the chemical potential of constituent i in its standard reference state (fcc Ca metal, bcc K metal etc.), and $\Delta\mu_i$ is the difference in chemical potential upon the crystallization of constituent i. The $\Delta\mu_i$ terms are constrained by the formation enthalpy of the $\mathrm{KCaI_3}$ compound. Specifically, the following constraints have to be satisfied for the formation of $\mathrm{KCaI_3}$.

$$\Delta\mu_{\mathrm{K}} + \Delta\mu_{\mathrm{Ca}} + 3\Delta\mu_{\mathrm{I}} = \Delta H_{\mathrm{KCaI_3}} \quad (4)$$

$$\Delta\mu_{\mathrm{K}} + \Delta\mu_{\mathrm{I}} < \Delta H_{\mathrm{KI}} \quad (5)$$

$$\Delta\mu_{\mathrm{Ca}} + 2\Delta\mu_{\mathrm{I}} < \Delta H_{\mathrm{CaI_2}} \quad (6)$$

$$\Delta\mu_{\mathrm{K}}, \Delta\mu_{\mathrm{Ca}}, \Delta\mu_{\mathrm{I}} < 0 \quad (7)$$

For the codoping impurities, we assume the formation of $\mathrm{MI_3}$ (M=La, Y, Gd, Sc) compounds as described in Ref. 41, or

$$\Delta\mu_{\mathrm{M}} + 3\Delta\mu_{\mathrm{I}} = \Delta H_{\mathrm{MI_3}} \quad (8)$$

To compensate for the spurious interactions between the defects in neighboring cells, we used the finite-size correction scheme based on a multipole expansion [41,42]

$$\Delta E_{\mathrm{f}}(L) = \Delta E_{\mathrm{f}}(L \to \infty) - \frac{\alpha_{\mathrm{Md}} q^2}{2\varepsilon L} - \frac{2\pi q Q}{3\varepsilon L^3} + O(L^{-5}) \quad (9)$$

where q is the charge of the defect, Q is the quadrupole moment, and the effective supercell size L is defined as the cubic root of the supercell volumes. The 1st-order term can be determined from the Madelung constant α_{Md} of the Bravais lattice of the supercell and the static dielectric constant of the material. The 3rd-order term is fit by calculated formation energies of the defects in 5 supercells with different sizes (40, 80, 160, 320 and 640 atoms respectively).

The exact position of the electron chemical potential μ_{e} is solved self-consistently by using the charged neutral constraint [40]:

$$n_{\mathrm{e}} - n_{\mathrm{h}} - \sum_i q_i c_i = 0 \quad (10)$$

where the index i runs over all the possible defects (both intrinsic and extrinsic), q_i is the charge of defect i, and c_i is the concentration solved by the Boltzmann distribution discussed above. n_{e} and n_{h} are the concentration of the free electron and holes, which follows Fermi-Dirac distribution. In the codoping case, an additional constraint needs to be applied,

$$\sum_i c_{\mathrm{M}i} = c_{\mathrm{M}} \quad (11)$$

where M=La, Y, Gd, or Sc, and the index i runs over all the possible defects related to codoping element M.

Finally, the thermodynamic transition energy is defined by the value of electron chemical potential at which the charge state of the vacancy switches from q_1 to q_2, and was calculated by

$$\Delta\epsilon_{\mathrm{th}}\left(\frac{q_1}{q_2}\right) = \frac{\Delta E_{\mathrm{f}}(q_1) - \Delta E_{\mathrm{f}}(q_1)}{q_2 - q_1} - \epsilon_{\mathrm{VBM}} \quad (12)$$

The calculated thermodynamic transition energies can be compared with the thermal trapping depth of various defects derived from our experimental thermoluminescence study.

RESULTS AND DISCUSSION

A. Optical Properties of the Grown Crystals

Figure 1 shows the single crystals of $\mathrm{KCaI_3:Eu^{2+}}$ codoped with different concentrations of $\mathrm{M^{3+}}$ (M=Sc, Y, Gd, or La) ions with different concentrations. All crystals are transparent, colorless, and inclusion-free except the 0.5% $\mathrm{Sc^{3+}}$ codoped sample, which has a brownish-red crystal surface. The measured concentrations of $\mathrm{Eu^{2+}}$ and codopants are listed in Table 1. The concentration of Eu in noncodoped and codoped samples was determined to be 1.4-1.7 at% except for 2.2 at% for the 0.5% Sc codoped sample. The codopant concentration in the crystal was found to be about 100 ppm for the 0.1 at% $\mathrm{M^{3+}}$ (M=Sc, Y, Gd, or La) codoped samples. The codopant concentration of Y, Gd, or La in the 0.5 at% $\mathrm{M^{3+}}$ codoped sample was 300-400 ppm. In contrast, the Sc concentration was determined to be 870 ppm in the 0.5 at% Sc codoped sample.

The optical absorption and RL spectra of $\mathrm{M^{3+}}$ (M=Sc, Y, Gd, or La) codoped $\mathrm{K(Ca_{0.97}Eu_{0.03})I_3}$ in the range of 350-800 nm are plotted in Figure 2. It is found that the shapes of the absorption spectra with and without codoping are almost the same. This suggests that these codopant will not induce color centers. For noncodoped $\mathrm{KCaI_3:Eu^{2+}}$, the RL emission maximum at 470 nm is associated with $\mathrm{Eu^{2+}}$ 5d-4f de-excitation, consistent with the previously reported result.[12] Only a slight blueshift of $\mathrm{Eu^{2+}}$ 5d-4f emission is observed in the codoped samples.

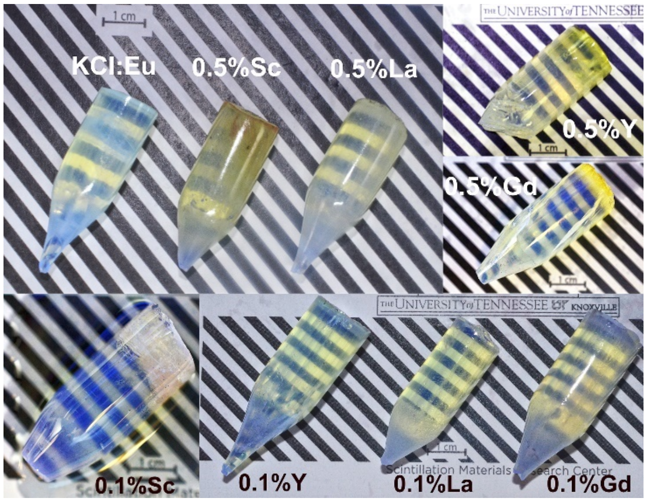

FIG 1. The noncodoped (upper left) and M^{3+} (M=Sc, Y, Gd, or La) codoped $KCaI_3:Eu^{2+}$ single crystals.

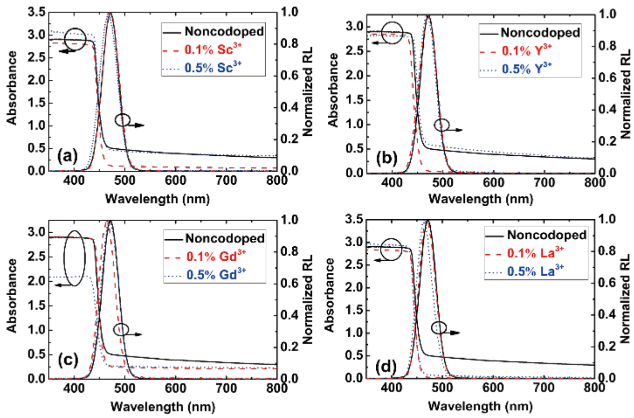

FIG 2. Optical absorption and RL spectra of 2 mm thick $KCaI_3:Eu^{2+}$ single crystals codoped with: (a) Sc^{3+}, (b) Y^{3+}, (c) Gd^{3+}, (d) La^{3+}. The absorption and RL spectra of noncodoped $KCaI_3:Eu^{2+}$ are shown for comparison in each figure.

B. Effects of codopants on Scintillation Properties

The scintillation decay profiles of 5×5×5 mm crystals of noncodoped and M^{3+} (M=Sc, Y, Gd, or La) codoped $KCaI_3:Eu^{2+}$ were measured. The decay profiles of Sc^{3+} codoped $KCaI_3:Eu^{2+}$ are shown in the Figure 3 inset for as examples. All of the decay profiles could be fit well by single exponential functions, and the constant decay data for all samples are presented in Figure 3 and Table 1. The decay constant of noncodoped $KCaI_3:Eu^{2+}$ is 1.1 µs, close to the result reported in Ref. 12. Decay time shortening is observed in all of the codoped samples, but the degree of impact relies on the codopant type and concentration. For instance, the reduction of decay time by tens ns is observed in Y^{3+}, Gd^{3+}, or La^{3+} codoped samples, but a more pronounced effect is seen in Sc^{3+} codoped samples, such as decreasing by approximately 300 ns for the 0.5 at% codoped sample compared to the noncodoped one.

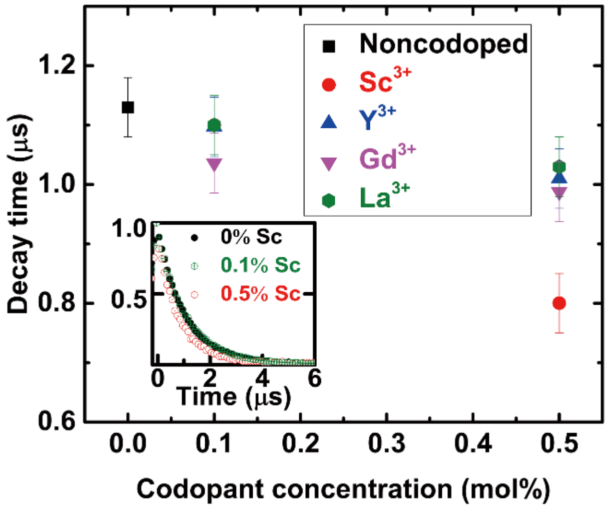

FIG 3. Scintillation decay time of noncodoped and M^{3+} (M=Sc, Y, Gd, or La) codoped $KCaI_3:Eu^{2+}$ single crystals acquired by a digital oscilloscope. Inset are the scintillation decay curves of $KCaI_3:Eu^{2+}$ codoped with different Sc^{3+} concentrations.

Scintillation afterglow is an important parameter in CT imaging, which requires at least three orders of magnitude reduction of afterglow in several milliseconds after X-ray cutoff. However, as a major obstacle, strong afterglow is a common feature for Eu^{2+} doped iodides. [10,13,22] X-ray induced afterglow profiles of noncodoped and M^{3+} (M=Sc, Y, Gd, or La) codoped $KCaI_3:Eu^{2+}$ are shown in Figure 4. For noncodoped $KCaI_3:Eu^{2+}$, the reduction in afterglow signal is only about one order of magnitude in the first three hours after X-ray cutoff. A beneficial effect on afterglow suppression is observed with Sc^{3+} codoping. The rate of initial decay increases after Sc^{3+} codoping and the afterglow level afterward decreases substantially, namely after hours the residual signal decreases by two orders of magnitude in the 0.1% Sc^{3+} codoped sample and three orders of magnitude in the 0.5% Sc^{3+} codoped sample. To the best of our knowledge, this is the first successful use of codoping to achieve an order of magnitude reduction of afterglow in Eu^{2+} doped metal halides, although the application-oriented requirements are still not satisfied. Interestingly, the Y^{3+}, Gd^{3+} and La^{3+} codopants, which have the same valence state as Sc^{3+}, exert an utterly opposite influence on the afterglow performance. Their enhanced afterglow signal is maintained throughout the entire measurement time region for several hours.

The effects of Sc^{3+}, Y^{3+}, Gd^{3+} and La^{3+} codopants on light yield and energy resolution were also evaluated. The energy resolution of noncodoped and codoped $KCaI_3:Eu^{2+}$ crystals at 122 and 662 keV was measured by irradiation with ^{57}Co and ^{137}Cs gamma-ray sources, respectively, by using a high quantum efficiency Hamamatsu R6231−100 PMT. The derived energy resolutions at 122 and 662 keV are listed in Table 1, and the pulse height spectra of noncodoped and Sc^{3+} codoped samples are shown in Figure 5. The noncodoped sample has an energy resolution of 6.3% at 122 keV and 3.25% at 662 keV, close to the reported values. [12] With Y^{3+}, Gd^{3+}, or La^{3+} codoping, the energy resolutions become much worse, such as 4-7% at 662 keV and 8-12% at 122 keV. For Sc^{3+} codoped samples, an energy resolution of 3.4% at 662 keV and 6.6% at 122 keV still can be obtained in the 0.1 at% Sc^{3+} codoped sample, but it is degraded to 7.8% at 662 keV and 12% at 122 keV when the Sc^{3+} content is increased to 0.5 at%. By considering the wavelength-weighted quantum efficiency of R2059 PMT for noncodoped and codoped $KCaI_3:Eu^{2+}$ (about 21.6%) the absolute light yields were estimated and presented in Table 1. Light yield as a function of codopant concentration is shown in Figure 6. An absolute light yield of 65,000±3000 photons/MeV is estimated for noncodoped $KCaI_3:Eu^{2+}$. Codoped samples have a decreased light yield of 50,000 - 60,000 photons/MeV.

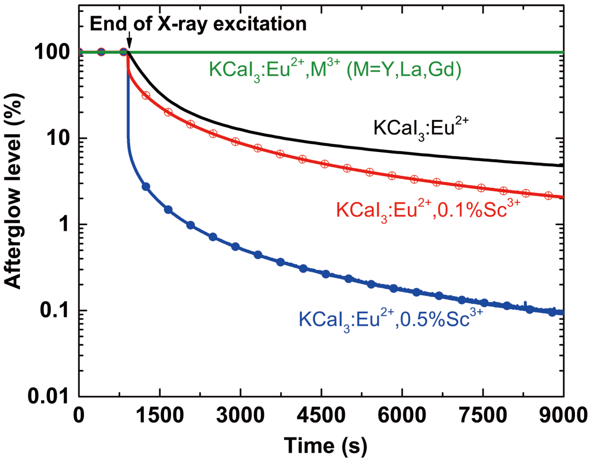

FIG 4. X-ray induced afterglow profiles of noncodoped and M^{3+} (M=Sc, Y, Gd, or La) codoped KCaI$_3$:Eu^{2+} single crystals.

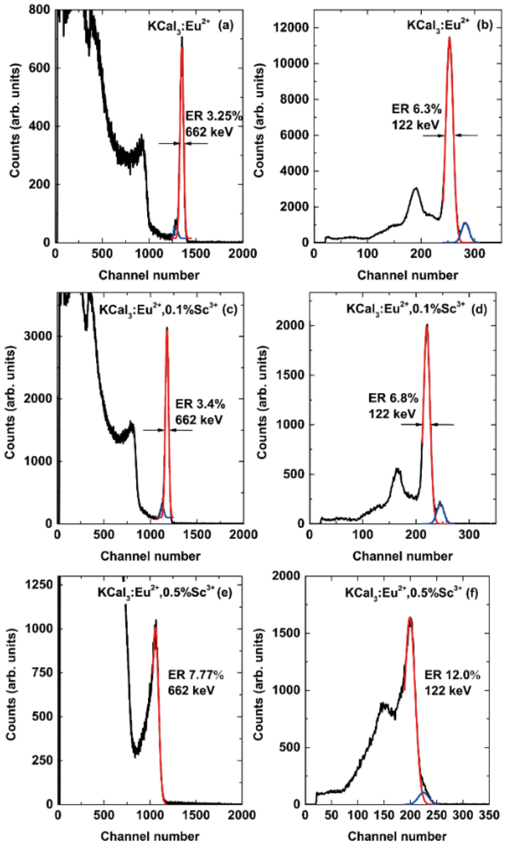

FIG 5. Pulse height spectra of noncodoped and Sc^{3+} codoped KCaI$_3$:Eu^{2+} crystals under ^{137}Cs or ^{57}Co source irradiation acquired by a Hamamatsu R6231-100 PMT.

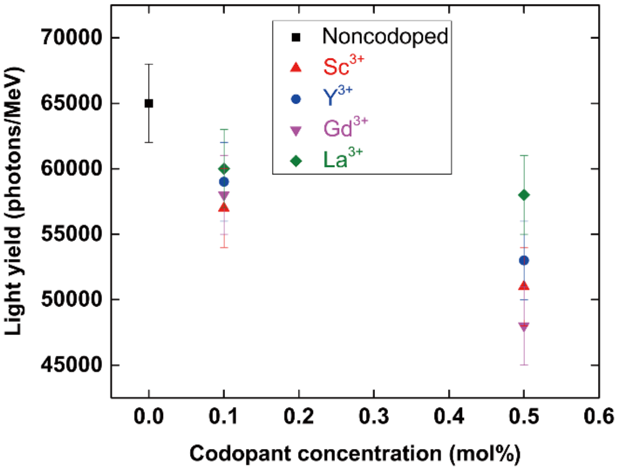

FIG 6. Absolute light yield of 5 mm cube noncodoped and M^{3+} (M=Sc, Y, Gd, or La) codoped KCaI$_3$:Eu^{2+} crystals.

Theoretically, the energy resolution is mainly determined by three factors: i) a statistical contribution from the variance in the number of photoelectrons produced in the PMT; ii) the degree of non-proportionality (nPR); and iii) the extent of inhomogeneity of LY response across the crystal and inhomogeneous light collection. [17] In the case of a high light yield scintillator the energy resolution is thought to be mainly influenced by nPR. Here, the codoped sample with lowest light yield still has about 50,000 photons/MeV. Consequently, a limited influence of statistical contribution on energy resolution is expected. To evaluate the contribution of nPR, the measured channel number of the full energy peak at each gamma-ray energy was determined. The data points were then normalized to the response at 662 keV. It can be observed from the nPR curves plotted in Figure 7 that codoping affects nPR in two general patterns. In the first case, seen in the Sc^{3+} and La^{3+} codoped samples, the nPR curves maintain nearly the same shape compared to the noncodoped sample. The second case, seen in the nonproportionality curves for Y^{3+} and Gd^{3+} codoped samples, involves a flattening of the "halide hump" with increasing codopant concentration as well as a greater deviation from the ideal line at lower energies. Despite the obvious difference, the calculated response deviation σ_{nPR} [43] only has a slightly difference between the noncodoped and codoped samples. It could be due to the limitation of predicting nPR solely by calculating σ_{nPR}. A more detailed investigation of the interaction between the excitations and the defects introduced into the system by codoping is required to explain the deterioration of the energy resolution of our codoped samples. However, the focus of this work is to provide an effective solution for suppressing the afterglow in KCaI$_3$:Eu and related halide scintillators, and a detailed analysis of nPR is beyond the scope of this paper.

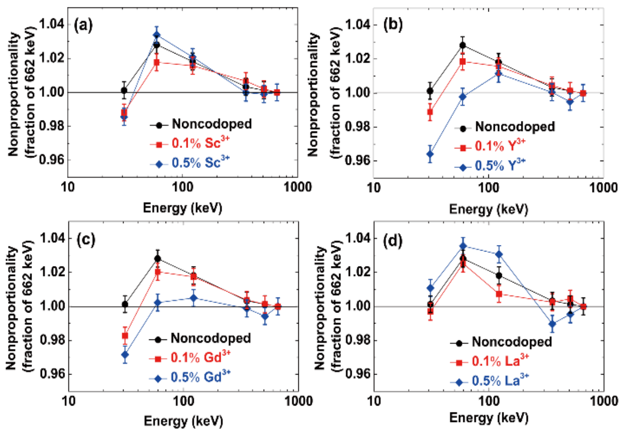

FIG 7. Nonproportionality responses of noncodoped and M^{3+} (M=Sc, Y, Gd, or La) codoped $KCaI_3$:Eu^{2+} (a) Sc^{3+}, (b) Y^{3+}, (c) Gd^{3+}, (d) La^{3+}. The nPR curve of noncodoped $KCaI_3$:Eu^{2+} is plotted in all figures for comparison.

TABLE I. Scintillation properties of noncodoped and M^{3+} (M=Sc, Y, Gd, or La) codoped $KCaI_3$:3 at%Eu^{2+} single crystals.

Composition	Eu^{2+} concentration (at%)		Codopant concentration (ppm)		RL emission (nm)	Light yield (ph./MeV)	Energy resolution (%)		Scint. decay (µs)
	In the melt	In the crystal	In the melt	In the crystal			122 keV	662 keV	
$KCaI_3$:Eu^{2+}	3	1.4	–	–	470	65,000±3000	6.3	3.25	1.13±0.05
$KCaI_3$:Eu^{2+},Sc^{3+}	3	1.7	1000	90	470	57,000±3000	6.6	3.4	1.10±0.05
	3	2.2	5000	870	468	51,000±3000	12.0	7.8	0.80±0.05
$KCaI_3$:Eu^{2+},Y^{3+}	3	1.7	1000	80	470	59,000±3000	8.3	4.2	1.11±0.05
	3	1.6	5000	290	469	53,000±3000	9.0	5.8	1.01±0.05
$KCaI_3$:Eu^{2+},Gd^{3+}	3	1.6	1000	90	466	58,000±3000	10.0	5.5	1.04±0.05
	3	1.4	5000	390	470	48,000±3000	10.7	6.1	0.99±0.05
$KCaI_3$:Eu^{2+},La^{3+}	3	1.6	1000	10	469	60,000±3000	7.5	4.0	1.10±0.05
	3	1.5	5000	290	464	58,000±3000	11.9	7.4	1.03±0.05

C. Defect Structure – Experimental and Theoretical Study

To explain the decay time shortening and afterglow variation after codoping, an understanding of the defect structures is indispensable because the defects will lead to localized trap levels within the band gap and the associated trapping effect will influence the energy transfer processes of free charge carriers. For instance, shallow traps can delay the electron/hole capture at the activator and result in a prolonged scintillation decay, and electron/hole detrapping from the populated deep traps after irradiation can give rise to afterglow. The afterglow mechanism of Eu^{2+} doped optical materials is related to electron trapping and releasing. Due to the electronic configuration of Eu^{2+}, it is likely to trap holes. Thus, the electrons freed from the traps located close to the conduction band will recombine at europium centers to generate Eu^{2+} emission. The thermoluminescence technique is used to experimentally study the thermal trapping depth and afterglow-related detrapping time in noncodoped and codoped samples.

Thermal trapping levels evaluated by thermoluminescence technique. The spectrally unresolved TL glow curves of M^{3+} (M=Sc, Y, Gd, or La) codoped $KCaI_3$:Eu^{2+} are shown in Figure 8 as along with that of the noncodoped sample. The noncodoped sample has TL maxima at temperatures of about 78, 106, 145, 183, 236, 296, 362, 383, and 491 K, and their positions are consistent with those previously reported. [13] Considering the variation of TL intensity with codoping, the entire TL glow curve could be divided into three temperature intervals:

i) Below 100 K, for all codoped samples there is an evident trend in decreasing TL intensity with increasing M^{3+} concentration. The diminishing and/or removal of corresponding shallow traps should be responsible for the decay time shortening phenomenon;

ii) Between 100 and 300 K, a clear decrease of TL intensity is also observed in all codoped samples, but is more pronounced in Sc^{3+} codoped samples;

iii) Above 300 K, Y^{3+}, Gd^{3+}, or La^{3+} codoping enhances the intensity of a TL peak at 380-400 K and induces TL peaks at higher temperatures. It explains the intensified afterglow performance and the reduced light yield in these codoped samples. In the case of Sc^{3+} codoping, the decrease of TL intensity by orders of magnitude with increasing Sc^{3+} concentration in comparison to the noncodoped sample contributes to the observed afterglow suppression at room temperature.

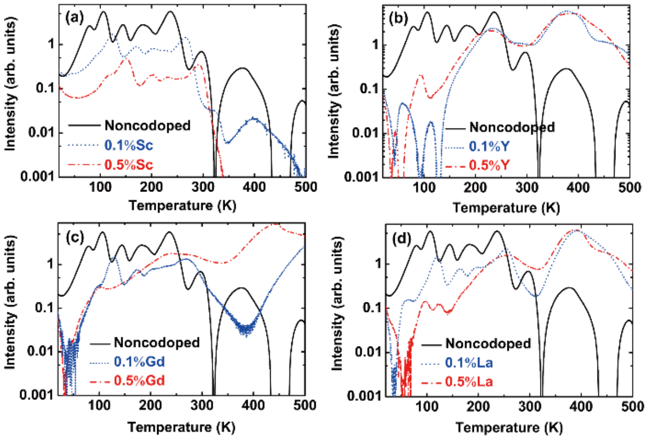

FIG 8. TL glow curves of $KCaI_3:Eu^{2+}$ crystals codoped with: (a) Sc^{3+}, (b) Y^{3+}, (c) Gd^{3+}, and (d) La^{3+} ions. The TL glow curve of noncodoped $KCaI_3:Eu^{2+}$ is shown in all figures for comparison.

To quantitatively investigate the thermal trapping levels in noncodoped and codoped samples, the parameters of the electron traps corresponding to TL peaks were obtained by analysing the glow curves. The similarity of TL curves of Y^{3+}, Gd^{3+}, or La^{3+} codoped samples implies an analogous effect of these codopants on structural defects. Thus, the TL glow curves of noncodoped, 0.1 at% Sc^{3+}, and 0.1 at% La^{3+} codoped $KCaI_3:Eu^{2+}$ were selected for study. Generally, the TL intensity I as a function of temperature T can be expressed as follows [44]

$$I(T) = sn_0 \exp\left(-\frac{E_t}{\kappa_B T}\right) \times \left[\frac{(l-1)s}{\beta}\int_{T_0}^{T} \exp\left(-\frac{E_t}{\kappa_B T}\right) dT + 1\right]^{-l/(l-1)} \quad (13)$$

Equation (13) is a general form of the TL intensity I, as a function of temperature T. In the above equations, n_0 is the initial occupied trap concentrations, E_t is the thermal trapping depth, κ_B is the Boltzmann constant, l is the kinetic order, s is the frequency factor, and β is the heating rate, 9 $Kmin^{-1}$ in this measurement. Because equation (13) cannot be directly used to fit the experimental data, the equation below was adapted in the fitting process [45].

$$I(T) = sn_0 \exp\left(-\frac{E}{k_B T}\right) \times \left\{\frac{(l-1)s}{\beta} \times T \times \exp\left(-\frac{E_t}{k_B T}\right) \times \left[\left(\frac{k_B T}{E_t}\right) - 2\left(\frac{k_B T}{E_t}\right)^2 + 6\left(\frac{k_B T}{E_t}\right)^3\right] + 1\right\}^{l(1-l)} \quad (14)$$

All three TL curves were well fitted by using ORIGIN 8 software, and plotted in Figure 9. The specific derived parameters are listed in Table 2. To correlate the traps with afterglow, the detrapping time τ of the trap at the temperature T can be calculated as [46]

$$\tau = s^{-1} \times e^{\frac{E}{kT}} \quad (15)$$

The calculated detrapping time for each trap at room temperature is also listed in Table 2. The noncodoped $KCaI_3:Eu^{2+}$ has deep traps located at 1, 1.07 and 1.5 eV below the conduction band minimum (CBM) with corresponding detrapping times in the order of 10^4, 10^5 and 10^{10} s. The first two deep traps should be responsible for the observed afterglow shown in Figure 4. The Sc^{3+} codoped sample has a deep trap located at 1.12 eV below the CB with a detrapping time of 10^5 s, but its initial occupied trap concentration drops by 83-87% compared to the trap in the noncodoped sample. In contrast, after La^{3+} codoping, the initial occupied trap concentrations of the deep trap with a depth of 1.07 eV increases by 77 times, and a new deep trap with a depth of 1.2 eV is formed, both of which contribute to the enhancement the afterglow of the sample.

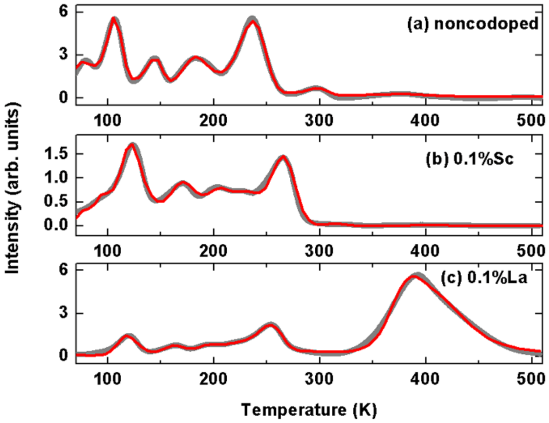

FIG 9. The fitted glow curves (red lines) and the experimental glow curves (grey lines): (a) noncodoped $KCaI_3:Eu^{2+}$, (b) 0.1% Sc^{3+} codoped $KCaI_3:Eu^{2+}$, and (c) 0.1% La^{3+} codoped $KCaI_3:Eu^{2+}$.

TABLE II. The peak temperature (T_m), initial occupied trap concentrations (n_0), the thermal trapping depth (E_{trap}), the frequency factor (s) and the detrapping time (τ) of $KCaI_3:Eu^{2+}$, $KCaI_3:Eu^{2+}$,0.1%Sc^{3+}, and $KCaI_3:Eu^{2+}$,0.1%La^{3+} samples

Samples	T_m (K)	E_{trap} (eV)	n_0	s (s^{-1})	τ at RT (s)
$KCaI_3$:Eu	78	0.12	795	3.1×10^6	3.4×10^{-5}
	106	0.17	259	3.5×10^6	1.9×10^{-4}
	145	0.25	101	1.9×10^7	6.8×10^{-4}
	183	0.31	167	1.3×10^7	1.0×10^{-2}
	236	0.40	254	1.9×10^7	3.0×10^{-1}
	296	0.72	16	1.3×10^{11}	1.1×10^1
	362	1.00	3	6.9×10^{12}	1.0×10^4
	383	1.07	4	7.4×10^{12}	1.2×10^5
	491	1.50	1.5	2.0×10^{14}	7.4×10^{10}
$KCaI_3$:Eu,0.1%Sc	76	0.12	10	5.0×10^5	2.1×10^{-4}
	90	0.14	63	9.0×10^5	2.5×10^{-4}
	123	0.20	134	9.9×10^6	2.4×10^{-4}
	171	0.27	54	5.0×10^6	7.3×10^{-3}
	203	0.31	29	2.8×10^6	6.4×10^{-2}
	228	0.30	35	5.0×10^6	2.4×10^{-1}
	265	0.56	62	3.2×10^9	9.0×10^{-1}

	324	0.87	1	7.4×10^{12}	5.6×10^{1}
	390	1.12	0.5	1.0×10^{13}	6.6×10^{5}
$KCaI_3$:Eu,0.1%La	120	0.17	113	7.3×10^{5}	9.5×10^{-4}
	164	0.26	39	5.4×10^{6}	4.1×10^{-3}
	196	0.29	47	1.9×10^{6}	4.4×10^{-2}
	222	0.35	33	3.2×10^{6}	2.1×10^{-1}
	250	0.40	163	2.8×10^{6}	1.7
	256	0.57	73	1.1×10^{10}	3.0×10^{-1}
	385	1.07	311	7.9×10^{12}	1.3×10^{5}
	423	1.20	64	1.2×10^{13}	7.6×10^{6}

From the TL experiments, it is not possible to directly identify the origin of individual electron trap. Hence, we employed the density functional calculations to determine the type of intrinsic and external defects, and to compare the calculated thermal trapping depth and defect concentrations with the results derived from TL study.

Thermodynamic boundary conditions. Applying the constraints on the relative chemical potentials and the formation enthalpies, the stability region of $KCaI_3$ is quite narrow [47]. This allows us to solve for the relative chemical potential of K and Ca respectively under the I-rich ($\Delta\mu_I = 0$ eV) and I-poor ($\Delta\mu_I = -2.68$ eV) limits.

Intrinsic defects. We consider all the possible intrinsic defects (vacancies, interstitials and antisites) in $KCaI_3$. The calculated formation energies with respect to electron chemical potential μ_e under both I-rich and I-poor conditions are shown in Figure 10. The μ_e ranges from zero to the calculated band gap E_G^{DFT}=3.66 eV and also the experimental band gap E_G^{exp}=5.32 eV [13] as shown in the gray area in Figure 10. Although there are two distinguishable iodine sites at Wyckoff positions I_1-8f, I_2-4c. The calculated formation energies of the associated defects at I_1 and I_2 sites are only separated apart by 30 meV at most. Therefore, we have shown only the defects with lower formation energies in Figure 10 for simplicity. However, defects related to both I_1 and I_2 sites are taken into consideration when we calculate the electron chemical potential based on the charge neutrality constraint. At the calculated μ_e illustrated by the vertical magenta line in Figure 10, we can readily see that the most important electron traps under both I-rich and I-poor conditions are Ca_K antisite and V_I vacancies.

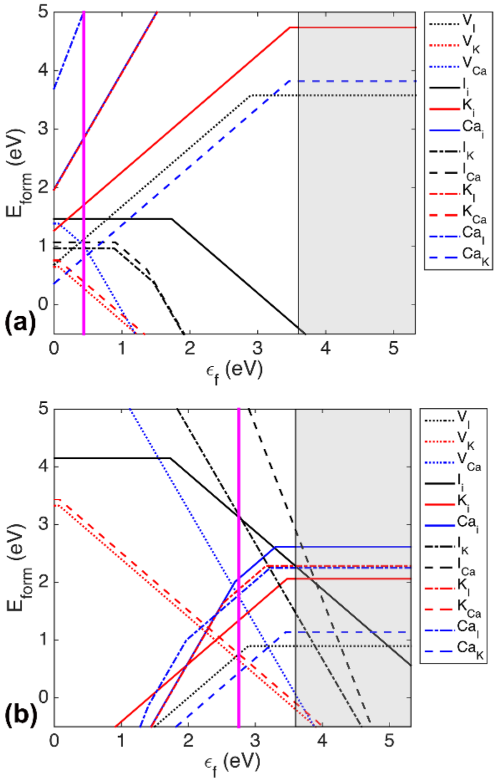

FIG 10. Calculated formation energies with respect to electron chemical potential μ_e of intrinsic defects in $KCaI_3$ under (a) I-rich condition and (b) I-poor condition. The vertical magenta line shows the calculated μ_e constrained by charge neutrality condition. The types of defects are listed in the legend. The gray area shows the data extended to the experimental band gap E_G^{exp}.

Codoping element related substitution and interstitial defects. The site occupation of the codopants deserves to be discussed. From the ionic radius standpoint, Y^{3+}, Gd^{3+}, and La^{3+} ions are expected to occupy the six-coordinated Ca^{2+} sites in $KCaI_3$. To be specific, comparing with the ionic radius of six-coordinated Ca^{2+} ions, the ionic radius difference ΔR, listed in Table 3, is 2% for Y^{3+}, 6.2% for Gd^{3+}, and 3.2% for La^{3+} ions, respectively. In contrast, the difference is five to ten times larger in comparison to the ionic radius of the eight-coordinated K^+ ion. However, the site occupation of Sc^{3+} ions is unable to be determined considering its large values of ΔR, 25.5% for Ca^{2+} substitution site and 42.4% for K^+ substitution site. Therefore, theoretical calculations were applied to clarify the site occupation of codopants by considering the formation energies.

TABLE III. Effective ionic radii of host and codopant ions, and the ionic radius difference between host and codopant ions.

	Ion	Ionic radius [48] (pm)		ΔR (%) b)	
		6 CN a)	8 CN	Ca^{2+} site	K^+ site
Host	K^+	-	151	-	-
	Ca^{2+}	100	-	-	-

Codopant	Sc^{3+}	74.5	87	25.5	42.4
	Y^{3+}	102	114	2	24.5
	Gd^{3+}	93.8	105.3	6.2	30.3
	La^{3+}	103.2	116.0	3.2	23.2

[a] "CN" represents coordination number.

[b] $\Delta R = |R_{host} - R_{codopant}| / R_{host}$

The formation energies of M_{Ca}, M_K substitution and M_i interstitial where M=La, Y, Gd, Sc are shown in Figure 11. Due to the significant ion radius mismatch between the Sc^{3+} and Ca^{2+} or K^+ ions, the formation energies of Sc_{Ca} and Sc_K substitutions are higher than the La/Y/Gd substitutions. On the other hand, Sc_i interstitial is clearly more energetically favorable than the interstitials formed by the other three codopants. To better understand this important difference, we illustrate the structure of La_i^{3+} and Sc_i^{3+} interstitials in Figure 12.

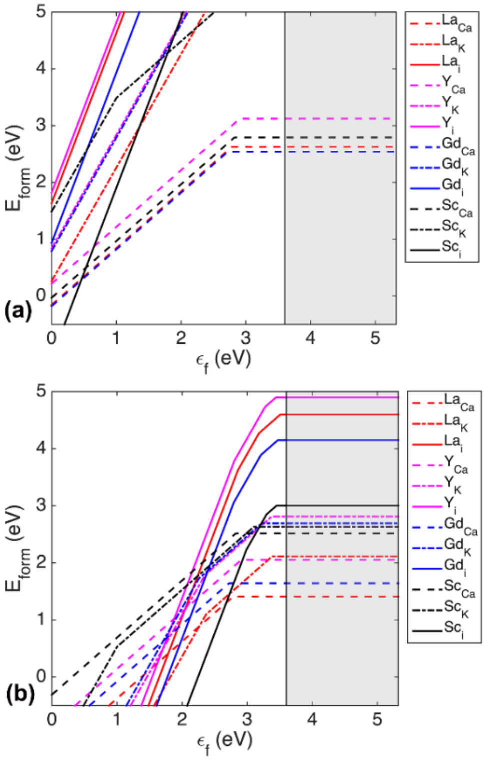

FIG 11. Calculated formation energies with respect to electron chemical potential μ_e of substitutional X_{Ca}, X_K and X_i interstitial (X=La, Y, Gd, Sc) in $KCaI_3$ under (a) I-rich condition and (b) I-poor condition. The types of defects are listed in the legend. The gray area shows the data extended to the experimental band gap E_G^{exp}.

As shown in Figure 12, the La_i^{3+} interstitial takes a "split form". The La^{3+} ion pushes the adjacent I^- and K^+ ions away and forms a nearly in-plane C_{3v} local structure with its three neighboring I^- ions. On the contrary, the Sc_i^{3+} interstitial takes a "tetrahedral form". The smaller Sc^{3+} ion undergoes less significant structural reconstruction to form the interstitial, therefore, the energy cost is much lower.

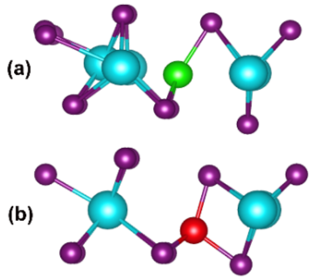

FIG 12. Local crystal structure of (a) La_i^{3+} and (b) Sc_i^{3+} interstitials. Green, red, purple, cyan spheres represent La, Sc, I, and K atoms respectively.

Codoping element related complex defects. As described in Ref. 41, a relatively low concentration of codoping may have a large impact on the defect formation and hence the luminescent properties of the scintillators through the formation of complex defects. Because all the substitution and interstitial defects introduced by the codoping elements are electron donors, it is reasonable to limit our study of the complex defects to those intrinsic defects forming acceptors. Due to the high formation energy of iodine interstitials and the fact that M_i+$V_{Ca/K}$ complexes are trivial, we concentrate our calculations on $M_{Ca/K}$+$V_{Ca/K}$ complex defects.

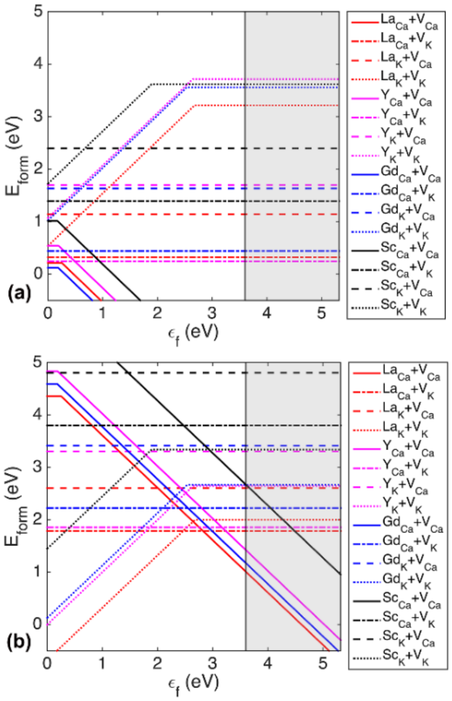

FIG 13. Calculated formation energies with respect to electron chemical potential μ_e of complex defects formed by a $M_{Ca/K}$ substitution and a $V_{Ca/K}$ vacancy (M=La, Y, Gd, Sc) in $KCaI_3$ under (a) I-rich condition and (b) I-poor condition. The types of defects are listed in the legend. The gray area shows the data extended to the experimental band gap E_G^{exp}.

As shown in Figure 13, the complex defects formed by $M_{Ca/K}$+$V_{Ca/K}$ for M=La, Y, Gd can be very energetically favorable, especially under the I-rich limit. It is worth noting that close to the I-rich limit, the dominant complex $M_{Ca}+V_{Ca}$ is an acceptor itself. If the formation energy of such a complex is so low (under this condition) that almost all the codoping ions form such structures under thermodynamic equilibrium, the codoping will act counter-intuitively in terms of controlling the Fermi-level and the charged defect concentration of the system. Under the I-poor limit, the formation energies of all types of the complex defects are higher due to the difficulty of forming cation vacancies under this condition. Similar complex defects were also believed to form in aliovalent and isovalent codoped SrI_2:Eu [49]. For Sc^{3+}, the complex defects are much less possible to form compared to the other three codopants, due to the high formation energies of forming substitutional $Sc_{Ca/K}$. Therefore, we can conclude that most of the Sc^{3+} dopants are likely to form Sc_i interstitials based on our calculation of the formation energies. Since Sc_i tend to exist as Sc_i^{3+}, which acts as a donor providing three extra electrons to the system per incorporated Sc, Sc codoping will push the Fermi level of the system closer to the CBM, favoring other acceptor-like defects to form and suppressing other donor-like defects. The quantitative effect of controlling the concentration of other charged defects is discussed later.

Thermal trapping depth of important electron traps estimated by theoretical calculation. As discussed earlier in the paper, important electron traps are the leading factor of the afterglow of our crystals. In Figure 14, we illustrate the thermodynamic equilibrium transition energy of electron traps with low formation energies. Our thermal trapping depth is defined as the energy difference between the current thermodynamic transition energy to the next transition energy level or the DFT calculated CBM.

Among the intrinsic defects, Ca_K is a shallow electron trap with a thermal trapping depth of 0.24 eV. Such a shallow trap can only contribute to the low temperature peaks in the thermal stimulated spectra. Iodine vacancies, on the other hand, is a relatively deep electron trap with a thermal trapping depth of 0.89 eV. As mentioned in the TL analysis section, a deep electron trap with a depth of ~ 1 eV is thought to be responsible for the afterglow observed. Therefore, it is reasonable to believe that the iodine vacancies are the main causes of the afterglow in $KCaI_3$:Eu^{2+}.

The M=Y, La, Gd codoping introduces a series of deep electron traps, and both M_{Ca} and M_K substitutions and the M_K+V_K complexes produce electron traps with depths ranging from 0.74 eV to 1.12 eV. These newly introduced defects can be added up and associated with the broadened bands over the 300 K regions in the TL glow curves. In fact, the newly formed deep electron traps were indeed found in these codoped samples, such as the trap with a depth of 1.2 eV corresponding to the TL peak at 423 K in the La^{3+} codoped sample.

Although the Sc_i interstitial defect is very likely to form based on our calculations of the formation energies, the electron thermal trapping depth is quite low as the deepest transition (+3/+2 → +2/+1) is only 0.27 eV. As a conclusion, Sc^{3+} codoping does not introduce any new deep electron traps to the system.

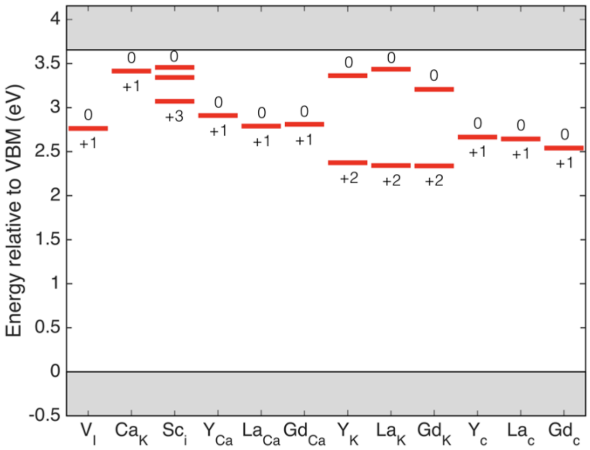

FIG 14. Thermodynamic equilibrium transition energies calculated for electron traps with low formation energies. Note that M_c means the M_K+V_K complex (M= Y, La, Gd) here in this figure.

Defect concentrations. In this section, we quantitatively study the movement of the electron Fermi level and the change in the concentration of the important electron traps in the system. We solve for the position of the Fermi level after all the codopant M^{3+} (M=La, Y, Gd, Sc) related defects are presented in the crystal based on the charge neutrality constraint, and the calculated Fermi levels with and without codoping for both I-rich and I-poor limits are listed in Table I. Since the effects of La, Y, and Gd codoping are similar, we only make a comparison between La and Sc codoping.

From Table 4 we can conclude that Sc_i is the most important defect in the case of Sc codoping, in which at least 71% of codoped Sc sites form Sc_i under all conditions. This makes the overall Sc codoping donor-like and shifts the Fermi level of the system toward the CBM, which reduces the concentration of other electron traps such as V_I vacancies by orders of magnitude within both the I-rich and I-poor limits. In addition, the Sc_i interstitials primarily formed have shallow thermal electron trapping depths.

In contrast, La (similarly Y and Gd) codoping shifts the Fermi level of the system toward the VBM due to the low formation energies of $La_{Ca}+V_{Ca}$ complexes, which favors the formation of intrinsic electron traps. Additionally, La/Y/Gd codoping also introduces new deep electron traps (mainly substitutional M_{Ca}) with remarkably high concentration as shown in Table 4. We expect the increased concentration of deep electron traps to broaden the thermoluminescence bands, and to enhance the afterglow of the crystal. This conclusion is consistent with the TL analysis.

TABLE IV. Calculated electron chemical potential (μ_e) shift, concentration of important electron traps under I-rich and I-poor conditions for none codoping (None), 0.1%Sc, 0.5%Sc, 0.1%La, and 0.5%La codoping cases, assuming system thermodynamic equilibrium at 797 K. Note that Sc codoping moves the μ_e toward the CBM and La codoping moves the μ_e towards the VBM.

	I-rich					I-poor				
	None	0.1%Sc	0.5%Sc	0.1%La	0.5%La	None	0.1%Sc	0.5%Sc	0.1%La	0.5%La
μ_e (eV)	0.437	0.464	0.499	0.348	0.277	2.753	2.857	3.056	2.737	2.695
c_{V_I} (cm^{-3})	1.18×10^{15}	6.43×10^{14}	1.64×10^{14}	4.61×10^{15}	1.33×10^{16}	2.58×10^{17}	3.84×10^{16}	3.04×10^{15}	2.99×10^{17}	5.44×10^{17}
c_{Sc_i} (cm^{-3})	0	3.90×10^{18}	1.69×10^{19}	0	0	0	4.70×10^{18}	2.10×10^{19}	0	0
$c_{La_{Ca}}$ (cm^{-3})	0	0	0	1.03×10^{18}	6.77×10^{18}	0	0	0	1.64×10^{18}	8.22×10^{18}
c_{La_K} (cm^{-3})	0	0	0	1.53×10^{14}	7.68×10^{14}	0	0	0	8.39×10^{17}	4.19×10^{18}
$c_{La_K+V_K}$ (cm^{-3})	0	0	0	5.52×10^{13}	7.07×10^{14}	0	0	0	2.10×10^{14}	7.85×10^{14}

D. Validity of the defect-engineering strategy

As proposed above, by intentionally codoping cations with smaller ionic radius with respect to the host ions to preferentially form the positive charged interstitials, the afterglow originated from deep electron traps, such as iodine vacancies, can be reduced or suppressed. To validate this defect-engineering strategy, another codopant ion with a similar ionic radius with Sc^{3+} will be selected to conduct the verification experiment. Moreover, to exclude a possible situation resulting from aliovalent codoping that the selected codopant ions prefer to occupy at substitution sites and form positive charged centers, which might play the same role as positive charged interstitials, we choose to use isovalent codoping. The Mg^{2+} ion was chosen as the codopant ion here because of the same valence state with the host ion Ca^{2+} and a close ionic radius with Sc^{3+} (72 pm for Mg^{2+} vs 74.5 pm for Sc^{3+} under 6 coordination number).

High quality Mg^{2+} codoped $KCaI_3:Eu^{2+}$ single crystals were grown by the Bridgman method. The as-grown codoped ingot is shown in Fig. 15(a) inset. Typical sample size is 5 mm× 5 mm× 5 mm. As observed in Fig. 15(a), the afterglow level of $KCaI_3:Eu^{2+}$ is reduced by three-folds plus throughout the entire time period after Mg^{2+} codoping. TL results shown in Fig. 15(b) indicate that the afterglow suppression should be related to the reduction of the deep traps corresponding the TL peaks above 350 K. These results confirm the validity of the model we proposed because only the interstitial Mg^{2+}_i can effectively suppress the formation of iodine vacancies, and then lead to a reduced afterglow, which cannot be achieved by the electrically neutral substitution Mg_{Ca}. Furthermore, in RL spectra shown in Fig. 15(c), the blueshift of Eu^{2+} 5d-4f emission of Mg^{2+} codoped samples is consistent with that observed in Sc^{3+} codoped samples. We interpret the blueshift by a perturbation of Eu^{2+} emission centers via the surrounding Sc^{3+}_i or Mg^{2+}_i. As presented in pulse height spectra shown in Fig. 15(d), the energy resolution at 662 keV slightly deteriorates from 3.25% for noncodoped sample, to 3.38% for 0.1 mol% Mg^{2+} codoped sample, and then to 3.6% for 0.5 mol% Mg^{2+} codoped sample.

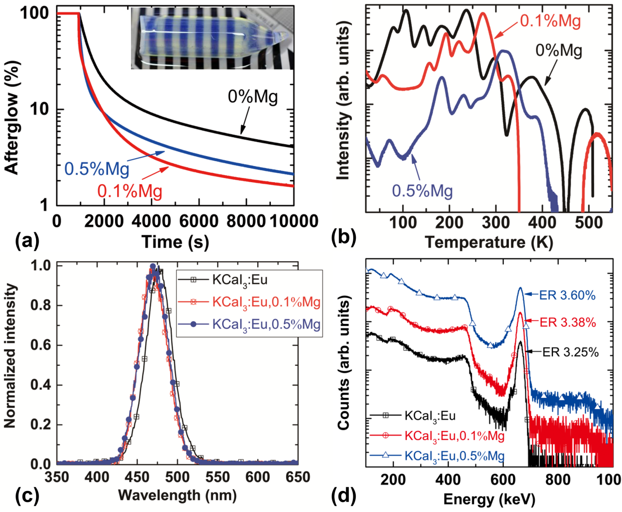

FIG 15. Scintillation properties of noncodoped, 0.1 mol% and 0.5 mol% Mg^{2+} codoped $KCaI_3:Eu^{2+}$ crystal samples: (a) X-ray induced afterglow profiles. Inset is an as-grown Mg^{2+} codoped $KCaI_3:Eu^{2+}$ ingot; (b) TL glow curves; (c) normalized RL spectra; and (d) pulse height spectra under ^{137}Cs source irradiation acquired by a Hamamatsu R6231-100 PMT.

IV. CONCLUSIONS

High quality M^{3+} (M=Sc, Y, Gd, or La) codoped $KCaI_3:Eu^{2+}$ single crystals were grown by the Bridgman method. Sc^{3+} codoping has beneficial effects on scintillation decay time and afterglow. Specifically, the scintillation decay time is shortened by tens to hundreds of ns, and the afterglow is suppressed by 1-2 orders of magnitude. For low-concentration Sc^{3+} doping, light yield of ~57,000 photons/MeV and energy resolution of ~3.4% at 662 keV can be maintained. Y^{3+}, Gd^{3+}, or La^{3+} codoping can also accelerate the scintillation decay time by tens of ns, but at the same time significantly enhance the afterglow intensity. It was found that high codoping concentrations significantly deteriorate light yield and energy resolution.

The main electron traps under both I-rich and I-poor conditions in $KCaI_3$ system are Ca_K antisites (as shallow electron traps) and iodine vacancies (as deep electron traps). The iodine vacancies with a thermal trapping depth of about 1 eV are responsible for the afterglow observed at room temperature in noncodoped $KCaI_3:Eu^{2+}$.

Sc_i is the most important defect in the case of Sc codoping. The afterglow suppression found in Sc codoping is because: i) the donor-like Sc_i will shift the Fermi level of the system toward the CBM, which reduces the concentration of other electron traps such as V_I vacancies by orders of magnitude; ii) the primarily formed Sc_i interstitials are shallow electron traps, and hence have a fast electron detrapping rate.

The prolonged afterglow at room temperature in La, Y, or Gd codoped samples was caused by two factors: i) La (similarly Y and Gd) codoping shifts the Fermi level of the system toward the VBM due to the low formation energies of La_{Ca}+V_{Ca} complexes, which favors the formation of intrinsic electron traps such as iodine vacancies; ii) La/Y/Gd codoping introduces new deep electron traps. These deep traps are also responsible for the reduced light yield.

A successful afterglow suppression achieved in isovalent Mg^{2+} codoped samples proved our proposed strategy that codoping a cation with a smaller ionic radius to intentionally form the positive charged interstitial can reduce the formation of halogen vacancies acting as deep electron traps.

The further optimization of Sc^{3+} or Mg^{2+} codoping is needed to reduce the afterglow to the level required for practical applications. Our method can be extended to other high performing scintillators in the perovskite ABX_3 family, provided that the crystal structure of the host can accommodate the cation codopant ions into interstitial sites, which can perform similarly to the Sc^{3+} or Mg^{2+} codoping in this work. Our discovery offers an important engineering approach for afterglow suppression, and enables the designing of scintillator materials for medical imaging applications to take a significant step forward.

ASSOCIATED CONTENT

Supporting Information

Figure S1. The phase diagram of $KCaI_3$ plotted as functions of $\Delta\mu_{Ca}$ and $\Delta\mu_K$.

AUTHOR INFORMATION

Corresponding Author

* E-mail: ywu52@utk.edu, caswyt@hotmail.com (Y. Wu), q.l.lawliet@gmail.com (Q. Li)

ACKNOWLEDGMENTS

This work has been supported by the US Department of Homeland Security, Domestic Nuclear Detection Office, under competitively awarded grant #2012-DN-077-ARI067-06. This support does not constitute an express or implied endorsement on the part of the Government.

REFERENCES

[1] G. Blasse, Scintillation Materials, Chem. Mater. **6**, 1465 (1994).

[2] M. J. Weber, Inorganic scintillators: today and tomorrow, J. Lumin. **100**, 35 (2002).

[3]http://www.nobelprize.org/nobel_prizes/physics/laureates/2013.

[4] G. F. Knoll, Radiation detection, and measurement, Wiley, 2010.

[5] M. Nikl and A. Yoshikawa, Recent R&D trends in inorganic single-crystal scintillator materials for radiation detection, Adv. Opt. Mater. **3**, 463 (2015).

[6] E. V. D. van Loef, P. Dorenbos, C. W. E. van Eijk, K. Krämer, and H. U. Güdel, High-energy-resolution scintillator: Ce^{3+} activated $LaBr_3$, Appl. Phys. Lett. **79**, 1573 (2001).

[7] N. J. Cherepy, G. Hull, A. D. Drobshoff, S. A. Payne, E. van Loef, C. M. Wilson, K. S. Shah, U. N. Roy, A. Burger, L. A. Boatner, W.-S. Choong, and W. W. Moses, Strontium and barium iodide high light yield scintillators, Appl. Phys. Lett. **92**, 083508 (2008).

[8] L. Stand, M. Zhuravleva, A. C. Lindsey, and C. L. Melcher, Growth and characterization of potassium strontium iodide: A new high light yield scintillator with 2.4% energy resolution, Nucl. Instrum. Methods Phys. Res., Sect. A **780**, 40 (2015).

[9] K. Yang, M. Zhuravleva, and C. L. Melcher, Crystal growth and characterization of $CsSr_{1-x}Eu_xI_3$ high light yield scintillators, Phys. Status Solidi (RRL) **5**, 43 (2011).

[10] Y. T. Wu, M. Zhuravleva, J. A. Johnson II, H. Wei, M. Koschan, and C. L. Melcher, Effects of melt aging and off-stoichiometric melts on $CsSrI_3:Eu^{2+}$ single crystal scintillators, Phys. Chem. Chem. Phys. **18**, 8453 (2016).

[11] Y. T. Wu, S. S. Gokhale, A. C. Lindsey, M. Zhuravleva, L. Stand, J. A Johnson II, M. Loyd, M. Koschan, and C. L. Melcher, Toward high energy resolution in $CsSrI_3/Eu^{2+}$ scintillating crystals: effects of off-stoichiometry and Eu^{2+} concentration, Cryst. Growth Des. **16**, 7186 (2016).

[12] A. C. Lindsey, M. Zhuravleva, L. Stand, Y. T. Wu, and C. L. Melcher, Crystal growth and characterization of europium doped $KCaI_3$, a high light yield scintillator, Opt. Mater. **48**, 1 (2015).

[13] Y. T. Wu, Q. Li, B. C. Chakoumakos, M. Zhuravleva, A. C. Lindsey, J. A. Johnson II, L. Stand, M. Koschan, and C. L. Melcher, Quaternary iodide $K(Ca,Sr)I_3:Eu^{2+}$ single-crystal scintillators for radiation detection:

crystal structure, electronic structure, and optical and scintillation properties, Adv. Optical Mater. **4**, 1518 (2016).

[14] Y. T. Wu, A. C. Lindsey, M. Zhuravleva, M. Koschan, and C. L. Melcher, Large-size $KCa_{0.8}Sr_{0.2}I_3:Eu^{2+}$ crystals: growth and characterization of scintillation properties, Cryst. Growth Des. **16**, 4129 (2016).

[15] Y. T. Wu, A. C. Lindsey, M. Zhuravleva, M. Koschan, and C. L. Melcher, Growth of inch-sized $KCa_{0.8}Sr_{0.2}I_3:Eu^{2+}$ scintillating crystals and high performance for gamma-ray detection, CrystEngComm **18**, 7435 (2016).

[16] K. Yang, M. Zhuravleva, and C. L. Melcher, Scintillation kinetics and thermoluminescence of $SrI_2:Eu^{2+}$ single crystals, J. Lumin. **132**, 1824 (2012).

[17] P. Dorenbos, Fundamental limitations in the performance of Ce^{3+}-, Pr^{3+}, and Eu^{2+}- activated scintillators, IEEE Trans. Nucl. Sci. **57**, 1162 (2010).

[18] K. S. Song, R. T. Williams, Self-Trapped Excitons, Springer, Berlin/ Heidelberg, Germany 2013.

[19] Q. Li, J. Q. Grim, K. B. Ucer, A. Burger, G. A. Bizarri, W. W. Moses, and R. T. Williams, Host structure dependence of light yield and proportionality in scintillators in terms of hot and thermalized carrier transport, Phys. Status Solidi RRL **8**, 346 (2012).

[20] M. S. Alekhin, J. T. M. de Haas, I. V. Khodyuk, K. W. Krämer, P. R. Menge, V. Ouspenski, and P. Dorenbos, Improvement of γ-ray energy resolution of $LaBr_3:Ce^{3+}$ scintillation detectors by Sr^{2+} and Ca^{2+} co-doping, Appl. Phys. Lett. **102**, 161915 (2013).

[21] D. Åberg, B. Sadigh, A. Schleife, and P. Erhart, Origin of resolution enhancement by co-doping of scintillators: Insight from electronic structure calculations, Appl. Phys. Lett. **104**, 211908 (2014).

[22] Y. T. Wu, L. A. Boatner, A. C. Lindsey, M. Zhuravleva, S. Jones, J. D. Auxier II, H. L. Hall, and C. L. Melcher, Defect engineering in $SrI_2:Eu^{2+}$ single crystal scintillators, Cryst. Growth Des. **15(8)** 3929 (2015).

[23] O. Sidletskiy, A. Vedda, M. Fasoli, S. Neicheva, and A. Gektin, Crystal composition and afterglow in mixed silicates: the role of melting temperature, Phys. Rev. Appl. **4**, 024009 (2015).

[24] C. Brecher, A. Lempicki, S. R. Miller, J. Glodo, E. E. Ovechkina, V. Gaysinskiy, V. V. Nagarkar, and R. H. Bartram, Suppression of afterglow in CsI:Tl by codoping with Eu^{2+} - I: Experimental, Nucl. Instrum. Methods Phys. Res., Sect. A **558**, 450 (2006).

[25] V. V. Nagarkar, C. Brecher, E. E. Ovechkina, V. Gaysinskiy, S. R. Miller, S. Thacker, A. Lempicki, and R. H. Bartram, Scintillation properties of CsI:Tl crystals codoped with Sm^{2+}, IEEE Trans. Nucl. Sci. **55**, 1270 (2008).

[26] Y. T. Wu, G. H. Ren, F. Meng, X. F. Chen, D. Z. Ding, H. Y. Li, and S. K. Pan, Ultralow-concentration Sm codoping in CsI:Tl scintillator: A case of little things can make a big difference, Opt. Mater. **38**, 297 (2014).

[27] Y. T. Wu, G. H. Ren, M. Nikl, X. F. Chen, D. Z. Ding, H. Y. Li, S. K. Pan, and F. Yang, $CsI:Tl^+,Yb^{2+}$: ultra-high light yield scintillator with reduced afterglow, CrystEngComm **16**, 3312 (2014).

[28] M. A. Spurrier, P. Szupryczynski, K. Yang, A. A. Carey, and C. L. Melcher, Effects of Ca^{2+} co-doping on the scintillation properties of LSO:Ce, IEEE Trans. Nucl. Sci. **55**, 1178 (2008).

[29] M. Nikl, K. Kamada, V. Babin, J. Pejchal, K. Pilarova, E. Mihokova, A. Beitlerova, K. Bartosiewicz, S. Kurosawa, and A. Yoshikawa, Defect engineering in Ce-doped aluminium garnet single crystal scintillator, Cryst. Growth Des. **14**, 4827 (2014).

[30] S. P. Liu, J. A. Mares, X. Q. Feng, A. Vedda, M. Fasoli, Y. Shi, H. M. Kou, A. Beitlerova, L. X. Wu, C. D'Ambrosio, Y. B. Pan, and M. Nikl, Towards bright and fast $Lu_3Al_5O_{12}$:Ce,Mg optical ceramics scintillators, Adv. Opt. Mater. **4**, 731 (2016).

[31] F. Meng, M. Koschan, Y. T. Wu, and C. L. Melcher, Relationship between Ca^{2+} concentration and the properties of codoped $Gd_3Ga_3Al_2O_{12}$:Ce scintillators, Nucl. Instrum. Methods Phys. Res., Sect. A **797**, 138 (2015).

[32] K. Kamada, M. Nikl, S. Kurosawa, A. Beitlerova, A. Nagura, Y. Shoji, J. Pejchal, Y. Ohashi, Y. Yokota, and A. Yoshikawa, Alkali earth co-doping effects on luminescence and scintillation properties of Ce doped $Gd_3Al_2Ga_3O_{12}$ scintillator, Opt. Mater. **41**, 63 (2015).

[33] Y. T. Wu, F. Meng, Q. Li, M. Koschan, and C. L. Melcher, Role of Ce^{4+} in the scintillation mechanism of codoped $Gd_3Ga_3Al_2O_{12}$:Ce, Phys. Rev. Appl. **2**, 044009 1 (2014).

[34] P. Giannozzi, S. Baroni, N. Bonini, M. Calandra, R. Car, C. Cavazzoni, D. Ceresoli, G. L. Chiarotti, M. Cococcioni, I. Dabo, A. D. Corso, S. de Gironcoli, S. Fabris, G. Fratesi, R. Gebauer, U. Gerstmann, C. Gougoussis, A. Kokalj, M. Lazzeri, L. Martin-Samos, N. Marzari, F. Mauri, R. Mazzarello, S. Paolini, A. Pasquarello, L. Paulatto, C. Sbraccia, S. Scandolo, G. Sclauzero, A. P. Seitsonen, A. Smogunov, P. Umari, and R. M. Wentzcovitch, QUANTUM ESPRESSO: a modular and open-source software project for quantum simulations of materials, J. Phys. Condens. Matter **21**, 395502 (2009).

[35] J. P. Perdew, K. Burke, and M. Ernzerhof, Generalized gradient approximation made simple, Phys. Rev. Lett. **77**, 3865 (1996).

[36] H. J. Monkhorst and J. D. Pack, Special points for Brillouin-zone integrations, Phys. Rev. B **13**, 5188 (1976).

[37] S.L. Dudarev, G.A. Botton, S.Y. Savrasov, C.J. Humphreys, and A.P. Sutton, Electron-energy-loss spectra and the structural stability of nickel oxide: An LSDA+U study, Phys. Rev. B **57**, 1505 (1998).

[38] V. Anisimov, F. Aryasetiawan, and A. Lichtenstein, First-principles calculations of the electronic structure and spectra of strongly correlated systems: the LDA+ U method, J. Phys. Condens. Matter **9**, 767 (1997).

[39] E. Şaşioğlu, C. Friedrich, and S. Blügel, Effective Coulomb interaction in transition metals from constrained random-phase approximation, Phys. Rev. B **83**, 121101 (2011).

[40] P. Erhart, D. Åberg, and V. Lordi, Extrinsic point defects in aluminum antimonide, Phys. Rev. B **81**, 195216 (2010).

[41] P. Erhart, B. Sadigh, A. Schleife, and D. Aberg, First-principles study of codoping in lanthanum bromide, Phys. Rev. B **91**, 165206 (2015).

[42] Q. Li, R. T. Williams, and D. Åberg, First principles calculations and experiments predictions for iodine vacancy centers in SrI_2, Phys. Status Solidi (b) **250**, 233 (2013).

[43] G. Bizarri, E. D. Bourret-Courchesne, Z. Yan, and S. E. Derenzo, Scintillation and optical properties of BaBrI:Eu^{2+} and $CsBa_2I_5$:Eu^{2+}, IEEE Trans. *Nucl*. Sci., **58**, 3403 (2011).

[44] D. W. Cooke, B. L. Bennett, E. H. Farnum, W. L. Hults, R. E. Muenchausen, and J. L. Smith, Thermally stimulated luminescence from x-irradiated porous silicon. Appl. Phys. Lett. **70**, 3594 (1997).

[45] H. Feng, D. Z. Ding, H. Y. Li, S. Lu, S. K. Pan, X. F. Chen, G. H. Ren, Annealing effects on Czochralski grown $Lu_2Si_2O_7$:Ce^{3+} crystals under different atmosphere. J. Appl. Phys. **103** 083109 (2008).

[46] Mc Keever, S. W. S. Thermoluminescence of Solids; Cambridge University Press: Cambridge, 1985.

[47] See Supplemental Material at [URL will be inserted by publisher] for [The phase diagram of the stability region of $KCaI_3$].

[48] J. A. Dean, Lange's handbook of chemistry, McGraw-Hill, Inc. New York, 1999.

[49] Q. G. Feng, and K. Biswas, Ramifications of codoping SrI_2:Eu with isovalent and aliovalent impurities, J. Appl. Phys. **120**, 213104 (2016).